Physics of Fluids

RESEARCH ARTICLE | JULY 07 2023

Dynamics of droplet coalescence on a vibrating vertical surface

Lei Xiangshu (雷祥舒) ; Liu Yingwen (刘迎文) ; Yang Peng (杨鹏); Laurent Royon ; Xiaofeng Guo

Physics of Fluids 35, 072102 (2023)
https://doi.org/10.1063/5.0157591

Physics of Fluids ARTICLE pubs.aip.org/aip/pof

Dynamics of droplet coalescence on a vibrating vertical surface

Cite as: Phys. Fluids **35**, 072102 (2023); doi: 10.1063/5.0157591
Submitted: 9 May 2023 · Accepted: 19 June 2023 ·
Published Online: 7 July 2023

Xiangshu Lei (雷祥舒),[1,2] Yingwen Liu (刘迎文),[1,a)] Peng Yang (杨鹏),[1] Laurent Royon,[2] and Xiaofeng Guo[2,a)]

AFFILIATIONS

[1]Key Laboratory of Thermo-Fluid Science and Engineering of MOE, School of Energy and Power Engineering, Xi'an Jiaotong University, Xi'an, Shaanxi 710049, People's Republic of China
[2]Université Paris Cité, CNRS, LIED UMR 8236, Paris F-75006, France

[a)]**Authors to whom correspondence should be addressed:** ywliu@xjtu.edu.cn and xiaofeng.guo@u-paris.fr

ABSTRACT

A mass-spring-damper theoretical model with a phenomenological equation is established to clarify the underlying physics of the dynamics of droplets on a vertical surface driven by vibration. It is found experimentally and theoretically that the phase shift between droplet and plate appears and peaks at a lower frequency for a larger droplet. At a certain frequency, two droplets could move in the opposite direction. Based on the phase shift mechanism, we propose a strategy aimed at promoting droplet coalescence. Compared to the necessity of precise control of frequency for resonance-induced events, the strategy accepts a higher tolerance for frequency, at which opposite-motion-induced droplet coalescence could occur. The optimal frequency where there is a maximum phase shift between two droplets is derived, and a large-bandwidth frequency range, which allows at least 90% maximum phase shift, is defined. The good agreement between the experimental and theoretical results collectively shows that the motion of the larger droplet is in the opposite direction to that of the smaller one only at large-bandwidth frequency range and the two droplets coalesce with high enough amplitude. Our findings are helpful for the utilization of vibrating surfaces for droplet removal.

I. INTRODUCTION

Vapor condensation is critical and common in urban environmental control,[1] power generation,[2] food processing,[3] as well as water recovery[4–6] and treatment.[7] Rising energy costs, environmental impact, and carbon emissions have aroused persistent concerns over energy conservation in condensation processes. Considering the important role that vapor condensing plays in industrial processes, a higher-performance design of vapor condensation would be positive from both an economic and environmental perspective.

Dropwise condensation (DWC) and filmwise condensation (FWC) are two common modes of vapor condensation. In DWC, discrete droplets nucleate, grow, and then coalesce on a cool surface. The extra surface that is not covered by droplets continues to achieve condensation. In FWC, the whole surface is covered by a continuous condensate film, which causes a rapid increase in thermal resistance. They could suffer from tenfold lower heat transfer coefficients (HTC) than in DWC.[8] Moreover, reducing the area of the drop-covered surface, as soon as nucleation begins, is the key to achieving higher overall condensation HTC. For DWC on a vertical surface, when the diameter of a droplet exceeds the capillary length, it can slide off by gravity. This entrains other droplets during the sliding and refreshes extra condensation surface exposed directly to vapor. Consequently, the key to enhancing DWC is to accelerate drop removal, which is harder on randomly oriented surfaces.[9]

Superhydrophobic surfaces have been developed to promote sliding, detachment, and combination of small droplets.[10,11] When two neighboring drops coalesce, a spontaneous jumping effect due to surface energy release is stimulated.[12] This is reported to enhance condensation by an order of magnitude in HTC as compared to DWC on an ordinary surface.[13] Various micro-/nanostructured superhydrophobic surfaces can be obtained by chemical (etching and oxidation) or mechanical techniques (additive manufacturing).[14] However, the durability of these surfaces remains an issue, as the structures and coatings tend to degrade rapidly under high temperature and humidity conditions as well as scale deposits. Moreover, from the point of view of condensate nucleation, hydrophobic surfaces require a higher degree of supersaturation than ordinary surfaces.[15] An increase in the overall performance is thus compromised, as a lower condensation source temperature is required. Therefore, the active removal of droplets from ordinary surfaces is highly desirable.

Vibration of the condensation surface is an effective active technique, which could overcome the above challenges. Droplet deformation and displacement driven by vibration are key mechanisms for promoting surface detachment. Depending on the direction, frequency, and amplitude of vibration, droplets behave differently. On a horizontal surface vibrating along its normal direction, a backward motion of droplet is observed when the vibration frequency is smaller than a quarter of the eigen frequency or within a narrow domain around 1.5 times eigen frequency.[16] On a vertical surface vibrating along its longitudinal axis, if the vibration frequency is equal to the resonance frequency of the droplet, a maximal deformation can be obtained. In addition, if the amplitude of vibration is high, the deformation can overcome the contact angle hysteresis and the contact line starts to move.[17,18] The higher the contact angle, the greater this effect. Vibration in the transversal direction of the condensation surface also enhances detachment from superhydrophobic surfaces. As shown in Figs. 1(b) and 1(c), vertically and horizontally oriented substrates with superhydrophobic treatment are investigated, respectively, by Moradi *et al.*[19] and Sun *et al.*[20] They achieved droplet detachment by high-amplitude vibration at the resonance frequency. Statistical results show a reduction in the average size of the departing droplet and a significant increase (by 8.6) in droplet sliding speed compared to non-vibrated ones.[21] Consequences on the condensation heat transfer enhancement are noteworthy: Heat transfer rate improves by more than 70% over the stationary case when longitudinal vibrations at 100 and 200 Hz are applied to a vertical hydrophobic surface with contact angle $\theta = 114° \pm 4°$ [Fig. 1(a)].[22] A further strategy for promoting the detachment of droplets of various sizes can be adopted with cyclic variable frequency vibration. Shedding events on a superhydrophobic surface increase by 120% with this strategy.[19] The positive effect of vibration on condensation has also been reported elsewhere.[23,24] A common feature of the above reports is that they are limited to a specific frequency strongly related to the drop size. This is due to the low damping effect from the reduced adhesion force between a hydrophobic surface and droplets. Careful adjustment of frequency is thus necessary, which also requires a complex power supply and signal processing system. Moreover, to the best of our knowledge, no literature studies the merging effect of two neighboring droplets driven by vibration.

Figure 1 summarizes how our study is distinguished from the previous ones. The present study aims to experimentally and theoretically investigate the dynamics of droplet vibration on a vertical surface, with particular focus on the phase shift between two neighboring droplets at large-bandwidth frequency. Based on the theoretical model, we propose an operating strategy to enhance the coalescence of droplets of different sizes to form larger droplets, which are more likely to fall. This approach is experimentally validated with a device designed to explore a large frequency spectrum. Advantages of our study include: ordinary surface without hydrophobic treatment, large bandwidth vibration instead of only the resonance frequency.

II. MATERIALS AND METHODS

A. Experimental setup

The experimental setup is shown schematically in Fig. 2(a). A sinusoidal signal is generated by a signal generator (CENTRAD GF 266) and then amplified by a TIRA Analog Amplifier BAA 120. A vibrator (TIRA TV-51110) is fed by the amplified signal to vibrate a plate along its vertical axis. The copper plate studied has a contact angle of about 96° [Fig. 2(b)], as measured by a contact angle system (KRÜSS DSA25B). For visualization, a high-speed camera (FASTCAM SA3) with a macro lens (Sigma MACRO 105 mm F2.8 EX DG OS HSM) records the vibration of droplets on the plate at 10 000 fps (frames per second). The whole system (plate, vibrator, and high-speed camera) is placed into a humidity-regulated hermetic chamber. A highly humid environment (98% RH) helps avoid the

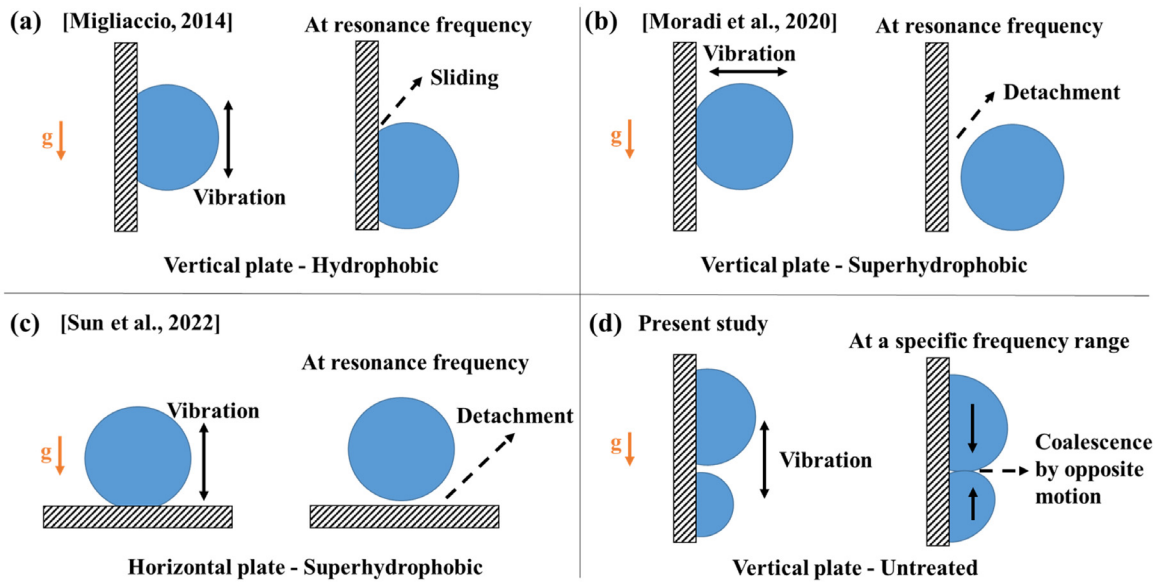

FIG. 1. Previous studies and the present study.

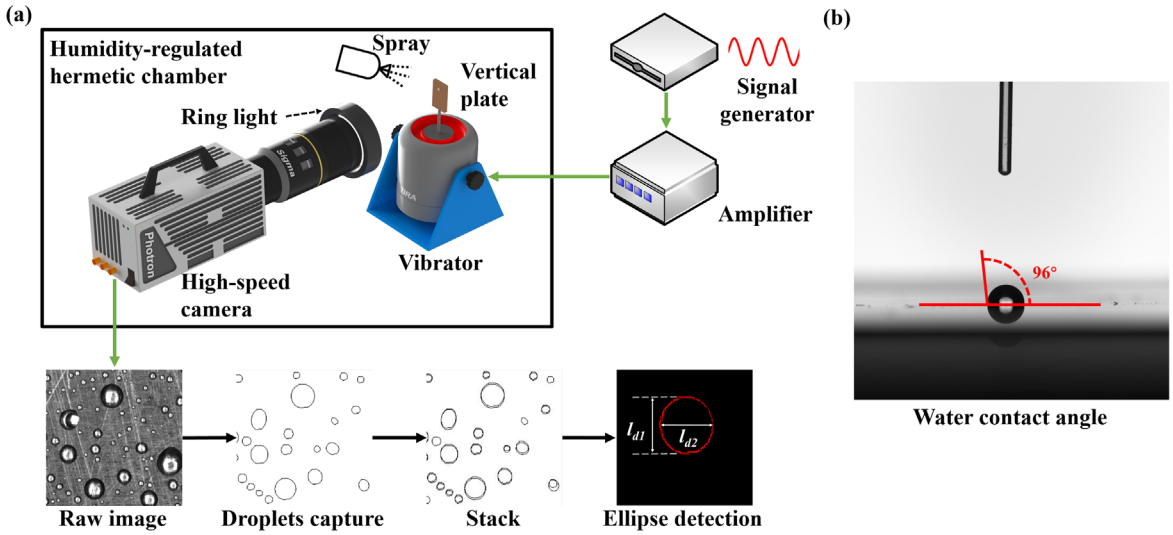

FIG. 2. (a) Schematic representation of the experimental setup. (b) Water-plate contact angle.

evaporation of droplets. The droplets on the plate are prepared by a sprayer, and their sizes depend roughly on the number of spraying.

B. Image processing procedure

Image processing is performed using ImageJ[25] and MATLAB.[26] Figure 2(a) shows the main procedure from raw image to drop morphology analysis. First, sequential images from the high-speed camera are converted to binary ones after sharpening, contrast conditioning, and threshold adjustment. This allows to capture the contours of the droplets. Then, two successive images, where the target droplets are in their highest and lowest positions, are stacked together. After that, we get a time-averaged elliptical contour of the target droplet. Finally, the stacked image containing only the target shape is processed with MATLAB to get the dimensions of the major (l_{d1}) and minor axes (l_{d2}). Similarly, the stacking method is used to obtain the length of a fixed point (l_p) on the plate, which gives the vibration amplitude. We define a dimensionless parameter AR (amplification ratio) to evaluate the displacement of the center of gravity of the droplet with respect to the plate:

$$\mathrm{AR}_e = \frac{l_{d1} - l_{d2}}{l_p}. \tag{1}$$

Depending on the frequency, there is a phase shift $\varphi_e \in [0, \pi]$ between the plate and a droplet. It is calculated from the difference between the two frames where the plate and the target droplet, respectively, start to move downward or upward:

$$\varphi_e = 2\pi \frac{\tau_p^i - \tau_d^i}{\tau_d^{i+1} - \tau_d^i}, \tag{2}$$

where τ represents the sequence of frame, and superscript i represents the ith cycle. For example, the frames where the droplet and plate reach the crest are chosen as standard frames. Then, the sequence of the standard frames for the ith and $(i+1)$th cycle is used to calculate φ_e in Eq. (2).

III. PHYSICAL MODEL OF A DROPLET SUBJECTED TO FORCED VIBRATION

A generally used model to describe the drop-surface movement is the mass-spring-damper system. Sarkar and Schowalter proposed a second-order ordinary differential equation (ODE) model to qualitatively describe the droplet motion.[27,28] We adapt this mass-spring-damper model to our situation to clarify the underlying mechanism of vibration-induced droplets motion (in particular, the phase shift between two droplets and their displacement). The vibrating droplet is illustrated in Fig. 3(a). We take the centroid of the droplet, without considering gravity, as the coordinate origin. Hence, in the steady state, droplets of different diameters have different displacements due to the influence of gravity. With limited plate displacement and at non-resonance frequency, the motion is the result of a balance between the driving force, F_d, the gravitational force, F_g, the restoring force, F_r, and the shear force when displacement occurs, F_dis. Accordingly, Newton's second law of drop movement writes

$$m_d \frac{\partial x_d^2}{\partial^2 t} = F_d + F_g + F_r + F_\mathrm{dis}. \tag{3}$$

The driving force between the wall and the droplet due to viscosity is a function of the velocity gradient and is expressed as follows:

$$F_d = \mu S_\cup \frac{\partial u}{\partial y} = \frac{\mu S_\cup}{\delta}(u_p - u_d), \tag{4}$$

where $\delta = \sqrt{\frac{2\nu}{\omega_p}}$ is the Stokes-layer thickness with ν the kinematic viscosity, $S_\cup = \frac{\pi d^2}{4}$ is the contact area between the bottom of the droplet and the plate, μ is the dynamic viscosity, $u_d = \frac{\partial x_d}{\partial t}$ is the velocity of the droplet, and $u_p = \frac{\partial x_p}{\partial t}$ is the velocity of the plate, where $x_p = X_p \sin(2\pi f_p t)$

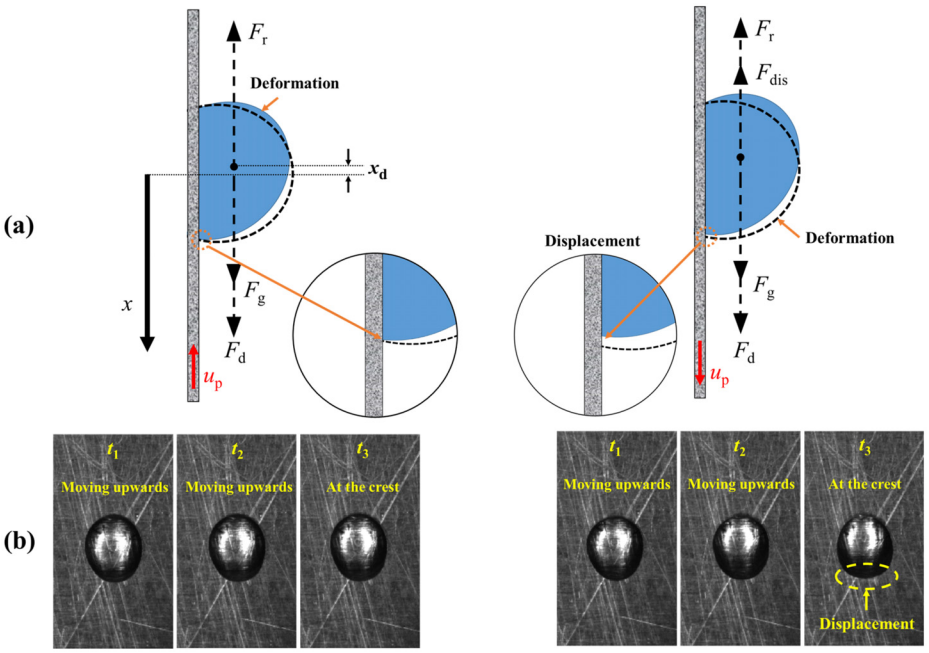

FIG. 3. (a) Schematic diagram of the force on a droplet without/with displacement. (b) Corresponding visualization images, left: deformation only and right: deformation + displacement.

is the equation of motion for the plate, with X_p the amplitude of vibration, m.

The gravitational force is expressed as follows:

$$F_g = m_d g = \rho V_d g. \tag{5}$$

With a given contact angle θ, the volume of the droplet V_d can be determined as follows:[29]

$$V_d = \frac{\pi d^3}{24}\left(\frac{2 - 3\cos\theta + \cos^3\theta}{\sin^3\theta}\right), \tag{6}$$

where d is the diameter of droplet measured according to the image from the high-speed camera.

The restoring force is calculated from the deformation of a droplet and is expressed as follows:[30]

$$F_r = -\frac{4\gamma S_\cap h}{d^2}(x_d - x_p), \tag{7}$$

where $S_\cap$ is the droplet surface area in contact with air at equilibrium state. It is determined as follows:

$$S_\cap = \frac{\pi d^2(1 - \cos\theta)}{2\sin^2\theta}. \tag{8}$$

In Eq. (7), h is a non-dimensional function depending on the wetting property of the surface. Celestini and Kofman[30] proposed a universal curve of h according to θ (°), expressed by the following equation:

$$h = -8e^{-7}\theta^3 + 8e^{-5}\theta^2 - 0.026\theta + 2.6589. \tag{9}$$

With driving frequency closer to the resonance frequency of the droplet and amplitude being high enough, droplet displacement could occur. Figure 3(b) shows images of a vibrating droplet without/with displacement. In the case of displacement, two issues are to be corrected in the model. First, as the amplitude increases, the hypothesis of a sufficiently weak external force does not hold.[30] Second, a shear force is applied to the droplet due to the relative motion at the droplet–wall interface. Sellier proposed a formula for the shear force by integrating the wall shear stress over the whole footprint of the droplet.[31] However, the no-slip condition and the constant droplet profile cannot apply when displacement occurs. Here, we propose a phenomenological equation expressed like a Gaussian distribution around the resonance frequency. The shear force due to displacement F_{dis} is described as follows:

$$F_{dis} = -\frac{\beta}{\varepsilon\sqrt{2\pi}} e^{\frac{-(f_p - f_r)^2}{2\varepsilon^2}}(u_d - u_p), \tag{10}$$

where f_r is the resonance frequency of the droplet.

The dimensional analysis implies that the units of β and ε are kg/s^2 and 1/s, respectively. Therefore, we define β as the additional tension at the resonant state, which is the product of the mass of the droplet and the square of its resonance frequency,

$$\beta = m_d f_r^2. \tag{11}$$

The parameter ε is the standard deviation representing the influence of the additional tension at resonance. Hence, we define ε as the efficient frequency. After fitting experimental results, we found that ε can be expressed as follows:

$$\varepsilon = \frac{f_r}{2}. \tag{12}$$

Substituting Eqs. (4), (5), (7), and (10) in Eq. (3) yields

$$m_d\frac{\partial x_d^2}{\partial^2 t} = \frac{\mu S_\cup}{\delta}\left[2\pi f_p X_p \cos\left(2\pi f_p t\right) - \frac{\partial x_d}{\partial t}\right] + m_d g - \frac{4\gamma S_\cap h}{d^2}x_d - \frac{\beta}{\varepsilon\sqrt{2\pi}} e^{\frac{-(f_p - f_r)^2}{2\varepsilon^2}}\left[\frac{\partial x_d}{\partial t} - 2\pi f_p X_p \cos\left(2\pi f_p t\right)\right]. \tag{13}$$

Equation (13) can be rewritten as follows:

$$m_d\frac{\partial x_d^2}{\partial^2 t}+\left(\frac{\mu S_\cup}{\delta}+\frac{\beta}{\varepsilon\sqrt{2\pi}}e^{\frac{-(f_p-f_r)^2}{2\varepsilon^2}}\right)\frac{\partial x_d}{\partial t}+\frac{4\gamma S_\cap h}{d^2}x_d = m_d g+\left(\frac{\beta}{\varepsilon\sqrt{2\pi}}e^{\frac{-(f_p-f_r)^2}{2\varepsilon^2}}+\frac{\mu S_\cup}{\delta}\right)2\pi f_p X_p\cos\left(2\pi f_p t\right). \quad (14)$$

Simplifying the equation, we get

$$\frac{\partial x_d^2}{\partial^2 t}+2p\frac{\partial x_d}{\partial t}+\omega_r^2 x_d = g+\frac{X'}{m_d}\cos\left(\omega_p t\right), \quad (15)$$

where the damping ratio p and resonance frequency ω_r are determined as follows:

$$p=\frac{\mu S_\cup+\frac{\beta\delta}{\varepsilon\sqrt{2\pi}}e^{\frac{-(f_p-f_r)^2}{2\varepsilon^2}}}{2\delta m_d}, \quad (16)$$

$$\omega_r=\sqrt{\frac{4\gamma S_\cap h}{m_d d^2}}. \quad (17)$$

$f_r=\frac{\omega_r}{2\pi}$ is the resonance frequency in Hz.

A new time-independent parameter, X', is used to simplify the above-mentioned expression, as follows:

$$X'=\left(\frac{\beta}{\varepsilon\sqrt{2\pi}}e^{\frac{-(f_p-f_r)^2}{2\varepsilon^2}}+\frac{\mu S_\cup}{\delta}\right)2\pi f_p X_p. \quad (18)$$

By solving Eq. (15) with initial conditions $u_d(0)=0$ and $F_r(0)=m_d g$, the analytical solution can be derived as follows:

$$x(t)=x_H(t)+x_P(t). \quad (19)$$

In the above-mentioned solution, $x_H(t)=e^{-pt}[C_1\cos(\omega_r' t)+C_2\sin(\omega_r' t)]$ is the homogenous solution with $\omega_r'=\sqrt{\omega_r^2-p^2}$. It approaches zero as the steady state achieves and this term could be neglected.

$x_P(t)=\frac{X'}{m_d\sqrt{(2\omega_p p)^2+m_d(\omega_r^2-\omega_p^2)^2}}\sin(\omega_p t+\varphi)+\frac{g}{\omega_r^2}$ is the particular solution representing the steady-state vibration, where $X_d=\frac{X'}{m_d\sqrt{(2\omega_p p)^2+m_d(\omega_r^2-\omega_p^2)^2}}$ is the amplitude of the droplet's center of gravity.

Theoretical phase shift φ_t is determined by the following equation:

$$\tan\varphi_t=\frac{-2\omega_p p}{\omega_r^2-\omega_p^2}. \quad (20)$$

Theoretical amplification ratio (the ratio of two amplitudes) is calculated by

$$\mathrm{AR}_t=\frac{X_d}{X_p}=\frac{l_{d1}-l_{d2}}{l_p}=\frac{2\sqrt{\pi}f_p\left(\beta e^{\frac{-(f_p-f_r)^2}{2\varepsilon^2}}+\mu S_\cup\right)}{\delta\varepsilon m_d\sqrt{8(\omega_p p)^2+2m_d(\omega_r^2-\omega_p^2)^2}}. \quad (21)$$

Finally, another critical parameter useful for droplets merging is the distance between the two borders (bottom of the upper drop and top of the lower one). The border positions are roughly calculated by $X_d-d/2$ with a circular shape hypothesis.

IV. RESULTS AND DISCUSSION

A. Experimental validation using the dynamic of single droplets

We begin by investigating the dynamics of individual droplets of three different sizes (1.00, 1.31, and 1.55 mm). Different exciting frequencies from 50 to 250 Hz are applied. The natural frequency of the three droplets is, respectively, 183, 122, and 95 Hz, inversely related to their size. For low frequencies, the motion of droplets is in phase with the plate due to the relatively higher surface tension ($\varphi=0$). Then, a phase shift φ starts to appear from a certain frequency (defined as starting frequency f_s). φ continues to increase rapidly until the input frequency reaches a sufficiently high value (defined as inversion frequency f_i). Beyond f_i, the droplet is completely in the opposite oscillation compared with the plate ($\varphi=\pi$). Figure 4(a) shows similar phase shift trends for the three droplet sizes. For each droplet, the starting and inversion frequencies, f_s and f_i, are close before and after their corresponding resonance frequency. Comparing experimental and theoretical results, the maximum theoretical phase shift φ_t is slightly smaller than that found experimentally. This is due to the deformation of droplet at high frequencies, which is not considered in the theoretical model. Globally, the way its trend and slope change with the input frequency, in good agreement with the experiment, validates the theoretical approach.

Figure 4(b) shows the amplification ratio of droplets compared with the plate oscillation amplitude. Both theoretical and experimental data show peak amplifications at around resonance frequency (183, 122, and 95 Hz). Under our conditions, the highest value of AR is about 6, implying much stronger drop motion than the plate. The amplification ratio remains higher than 5 at a bandwidth of ~10 Hz around the resonance frequency. The high AR at the large-bandwidth frequency is a valuable condition to achieve drop shedding or coalescence. We discuss about it later with two droplets dynamics.

In sum, experimental results fit well with theoretical ones in terms of amplification ratio and phase shift between single droplets and plate. Considering the consistency between the theoretical and experimental data, the theoretical model can be used to predict the motion of droplets in broader conditions. The following results are based on the validated theoretical model to study the behavior of neighboring droplets.

B. A strategy to promote coalescence of adjacent droplets

Figure 5 is obtained by applying the theoretical model to five droplet sizes from 1.00 to 1.40 mm. As shown in Fig. 5(a), larger droplets are more sensitive to lower frequencies due to their low resonance frequency. The starting frequency f_s and inversion frequency f_i are lower than smaller droplets. An exciting consequence is that at some specific frequency, a smaller droplet can be almost in phase with the plate, while a larger one is in the opposite phase. This provides condition (necessary but not sufficient) for adjacent droplets to merge. In addition, the slope of the curve rises with the increase in diameter because the damping ratio p decreases for larger drop sizes.

Figure 5(b) gives the theoretical phase shift between pairs of two droplets, using the 1.00 mm one as a reference. The phase shift

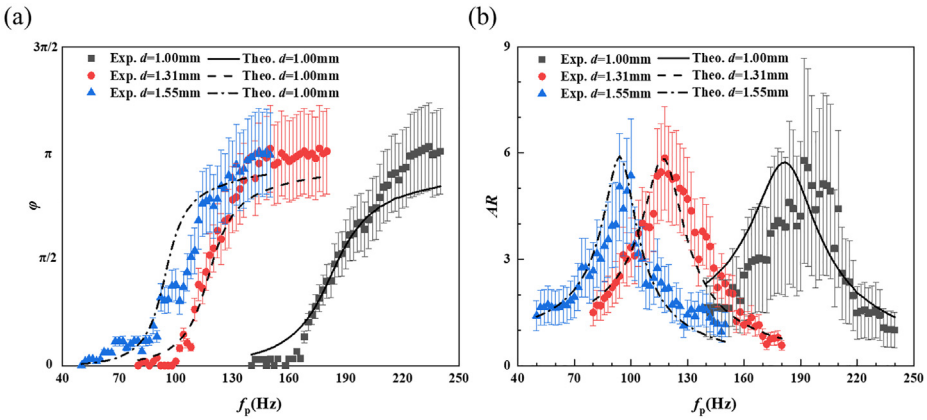

FIG. 4. Comparisons between theoretical (Theo.) and experimental (Exp.) results. (a) Phase shift. (b) Amplification ratio. Good agreement can be found for large droplets. For the smallest droplet at $d = 1.00$ mm, the experimental AR curve shifts to the right. This is due to the influence of evaporation during the experiment.

between two droplets, $\Delta\varphi$, starts to be significant for larger droplets who have lower resonance frequencies. Then, $\Delta\varphi$ reaches its peak value before decreasing at higher frequencies. The frequency corresponding to the peak phase shift is the optimal frequency f_{opt} to promote drop merging. For smaller droplets that are closer to the reference size, the phase shift frequency range is narrower. Moreover, the peak phase shift value decreases: It is $(3/4)\pi$ for the largest droplets pair (1.40 and 1 mm, near opposite motion), while only $(1/3)\pi$ for the pair 1.10 and 1 mm. We define the continuous frequency plateau where at least 90% $\Delta\varphi_{max}$ is satisfied as bandwidth. For example, between two droplets (1.10 and 1.40 mm), $f_{opt} = 133$ Hz. $\Delta\varphi$ around f_{opt} is a relatively large plateau. The whole range of [121, 146] Hz allows at least 90% maximum phase shift $\Delta\varphi_{max}$. The larger of this bandwidth corresponds to ± 12.5 Hz or $\pm 9.4\%$ f_{opt}. Compared to the resonance-induced shedding, our technique offers a larger bandwidth frequency at which two neighboring droplets could coalesce. For example, Sun *et al.* investigated the droplet detachment on a superhydrophobic surface at resonant vibration.[20] At the lowest amplitude, the frequency range should be kept within $\pm 1\%$ of its resonance frequency ($< \pm 1$ Hz). Out of this range, the vibration surface should be amplified by $+10\%$ of the lowest amplitude. The operational bandwidth of our study is thus much larger.

To generalize the theory in search of the best operational condition for different drop sizes, we determine the theoretical optimal frequency f_{opt}. At this frequency, the phase shift reaches its peak value $\Delta\varphi_{max}$, [c.f. Fig. 5(b)]. Ideally, $\Delta\varphi_{max}$ between two droplets would be π,

$$\left|\arctan\frac{-2\omega_{opt}p}{\omega_1^2-\omega_{opt}^2}-\arctan\frac{-2\omega_{opt}p}{\omega_2^2-\omega_{opt}^2}\right|=\pi. \tag{22}$$

The optimal frequency $f_{opt} = \omega_{opt}/2\pi$ can be obtained by

$$\omega_{opt}=\sqrt{\frac{d_1\omega_1^2+d_2\omega_2^2}{d_1+d_2}}. \tag{23}$$

The theoretical optimal frequencies of 22 drop size combinations are given in Fig. 6(a). The corresponding droplet sizes are $d_1 \in [1.2, 1.5]$ mm and $d_2 \in [0.8, 1.4]$ mm. One take-away message is that the optimal frequency lies between the two resonance frequencies for each droplet. Furthermore, the phase shift between two droplets ($\Delta\varphi$) at the corresponding optimal frequency decreases as the sizes of the two droplets get similar, as listed in Table I. It is thus difficult to achieve an absolute opposite movement for droplets with similar sizes. It is worth noting when $d_1 = d_2$, there is no way to force them into contact by the proposed vibration technique, since they are strictly in phase whatever the frequency is.

In addition to $\Delta\varphi$, we also need a high enough AR to promote droplets merging. Figure 6(b) shows the spectral distribution of AR for

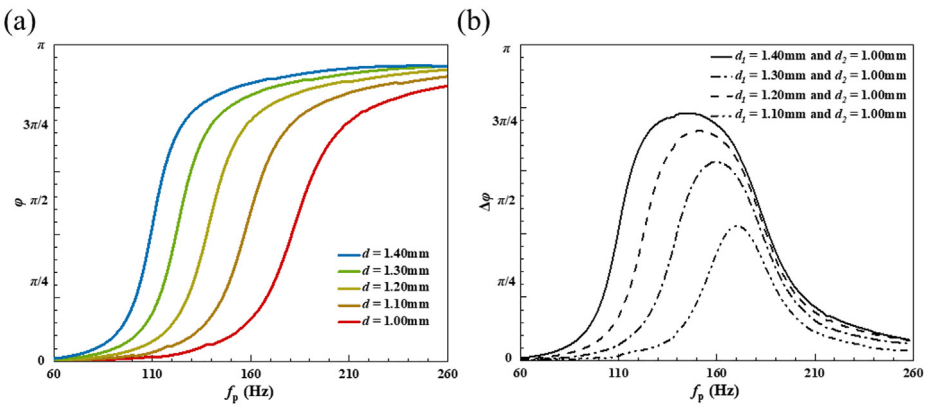

FIG. 5. (a) Phase shift between droplet and plate. (b) Phase shift between two adjacent droplets.

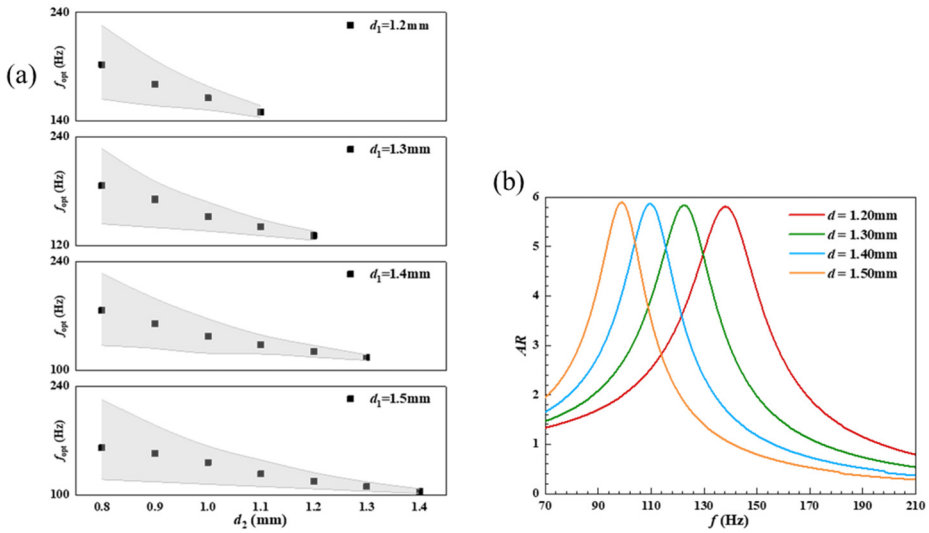

FIG. 6. (a) The optimal frequency in favor of droplet coalescence according to drop size combination. Shaded area shows the bandwidth around the optimal frequency satisfying 90% $\Delta\varphi_{max}$. (b) The frequency dependence of amplification ratio (AR) for different droplets.

four typical drop sizes. Peak AR values correspond to the resonance frequency of one specific drop size and are generally around 6 with our surface wetting conditions. According to the size combination, the optimal working frequency will not be at one specific resonance frequency, but in between the two resonance ones. Consequently, the AR is always lower. Fortunately, the operating frequency can be adjusted within the 90% optimal frequency range without strong disturbance to the relative phase shift $\Delta\varphi$. For instance, Fig. 6(a) indicates that an optimal frequency between a 1.2 mm drop and a 1.5 mm one should be at 118 Hz and the corresponding 90% optimal frequency range is from 108 to 129 Hz. At this frequency, Fig. 6(b) gives ARs of around 3.2 and 2.3 for the two droplets, respectively. If we fix the operating frequency at 108 Hz, the two ARs will be 2.4 and 3.9, which holds greater potential for droplet merging.

Eventually, we can define the scope of application of the strategy in terms of size limit and frequency limit. The study by Weisensee *et al.* points out that water droplets grow mainly via coalescence instead of direct condensation once their diameter is larger than the effective transition one at ∼20 μm.[32] With the current surface condition, theoretically it corresponds to a frequency limit of 65 kHz. The upper limit drop size can be obtained by balancing the gravitational and surface tension forces.[33] The average drop departure size for our surface is estimated to be ∼1.60 mm. The corresponding frequency (lower frequency limit) is ∼90 Hz.

TABLE I. Maximum phase shift between two droplets ($\Delta\varphi_{max}$) at the corresponding optimal frequency.

d_2 (mm) \ d_1 (mm)	1.20	1.30	1.40	1.50
0.80	0.82π	0.85π	0.87π	0.89π
0.90	0.75π	0.80π	0.84π	0.86π
1.00	0.63π	0.73π	0.78π	0.82π
1.10	0.40π	0.60π	0.71π	0.77π
1.20		0.38π	0.58π	0.69π
1.30	0.38π		0.34π	0.56π
1.40	0.58π	0.34π		0.34π

C. Application of the new operating strategy

We use a syringe to create droplets with controllable diameters and relative position. Specifically, a smaller droplet with a diameter of 1.12 mm and a larger one with a diameter of 1.39 mm are attached to a plate. They are aligned along the vibrating direction. The relative position of them in the x direction is 1.50 mm (center-to-center). Sinusoidal vibrations of different frequencies and amplitudes are applied to the plate, and the corresponding motions of the two droplets are visualized. Slow-motion videos showing the behaviors of the two droplets at different frequencies can be found in Fig. 7 (Multimedia view).

The resonance frequencies f_r for the two droplets are 154 and 112 Hz, respectively. Our theoretical model gives an optimal frequency f_{opt} at 132 Hz and a 90% satisfactory range from 121 to 143 Hz. During the experiment, we adopt three excitation frequencies at 80, 140, and 260 Hz. Theoretically, the 140 Hz one is within the optimal range, while 80 and 260 Hz would be either too low or too high. For $f_p = 140$ and 260 Hz, the amplitude of plate X_p is set to 0.042 mm. For $f_p = 80$ Hz, the amplitude of the plate X_p is set to 0.085 mm. Based on the amplitude and frequency of the plate, the motion profiles of the two droplets are given in Fig. 7. We distinguish the upper and lower limits of each droplet as well as their centers of gravity. The motion of the plate is also given. For merging purpose, special attention should be paid to the lowest limit of the upper droplet (larger one in our case) and the highest point of the bottom droplet (smaller one). The experimental keyframes are inset in the corresponding figures. At $f_p = 80$ Hz, the movements of the two droplets are almost synchronous with the movement of the plate. Therefore, the blank region between the two droplets indicates that they are in phase and cannot merge. Even if increasing the amplitude X_p, it has little effect on the blank region. At $f_p = 260$ Hz, the responses of the two droplets to the vibration of plate

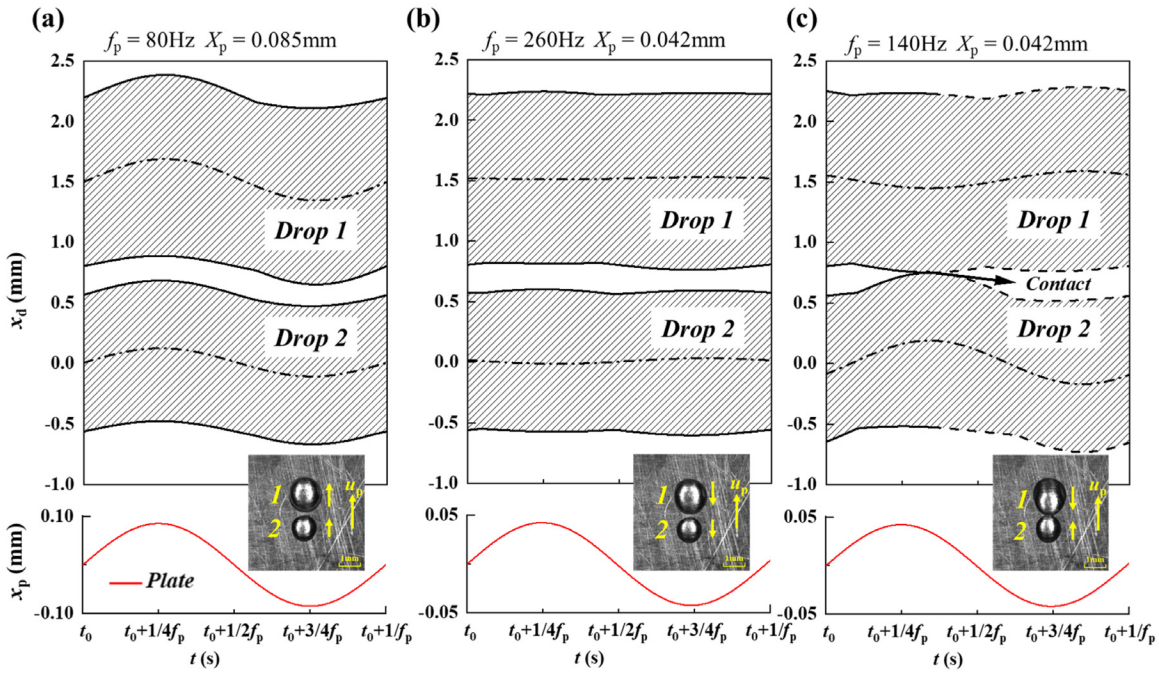

FIG. 7. Theoretical motion curves of two droplets and experimental keyframes at different frequencies. Shaded region represents the droplet projection on the plate, and dash-dotted line represents the motion curve of centers of gravity. Red lines represent the motion curve of the plate. Multimedia available online.

are weak. The blank region still exists due to gentle fluctuation of two droplets and small phase shift $\Delta\varphi$.

When $f_p = 140$ Hz, the two droplets are in totally reversed phase. The highest point of the smaller droplet and the lowest point of the larger droplet may come into contact when the plate is near the peak. The reason is that the larger droplet nearly asynchronous to the plate moves downward, while the smaller one nearly synchronous to the plate moves upward. This produces a contrary motion, which brings them together. Once the two droplets encounter each other, they merge rapidly and in an irreversible way.[34]

The process of contact is also observed in the experiment, as shown in the keyframe in Fig. 7(c). It should be noted that the dashed line after contact represents the virtual motion because the two droplets coalesce into a new one.

In addition to choosing the right frequency band, high enough amplitude is also a condition to achieve droplet merging. Figure 8 (Multimedia view) shows the motion of the two droplets (x_d) driven by the plate (x_p) at three different amplitudes. The frequency is fixed and within the optimal frequency band. As illustrated, the motion of the larger droplet (drop 1) is nearly opposite to the plate motion, while the smaller one (drop 2) is nearly synchronous to the plate. This property does not change as long as the frequency is fixed. At low vibration amplitude $X_p = 0.022$ mm, the responses are so mild that the two droplets remain separated. As X_p increases to 0.033 mm, the minimum distance between the two droplets reduces significantly, but the two droplets still do not contact. When X_p increases to 0.042 mm, their reactions further intensify so that they merge into one droplet spontaneously at the moment of approaching.

V. CONCLUSION

The dynamics of droplet coalescence driven by vibration on a vertical surface are experimentally and theoretically investigated. A phenomenological equation is introduced into a mass-spring-damper theoretical

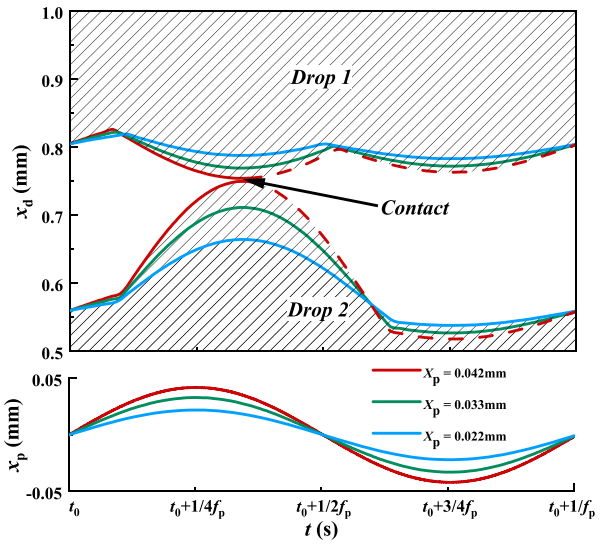

FIG. 8. Theoretical motion curve of the two droplets at different excitation amplitudes from the plate. For drop motion x_d, only the close border lines are shown, i.e., lower limit of drop 1 and upper limit of drop 2. The dashed lines are virtual as merging already occurs. Multimedia available online.

model to solve two problems: strong external force and additional shear force due to unpredicted slip of droplet footprint area. The results show that phase shift φ occurs from size-dependent starting frequencies f_s to inversion frequencies f_i. This leads to specific optimal frequencies at which two droplets of different sizes move in opposite directions. Coupled with a high enough amplitude, these droplets may furtherly coalesce. The working frequency bandwidth is at the order of ± 10 Hz or higher, offering more chances to promote coalescence of adjacent droplets.

Our findings could be helpful for the coalescence and removal of droplets. Given the droplets' size on the vertical surface, the optimal frequency can be obtained and then the vibration at the large-bandwidth frequency can be applied on the surface. The droplets coalesce and form a larger droplet, which could detach from the surface. During the sliding, the droplet entrains other drops, acting as wipers. Therefore, larger uncovered surface is made available for an intensified condensation effect. Furthermore, no special hydrophobic requirement is necessary for the surface. With certain frequencies applied on the surface, the droplets of different sizes can coalesce and detach much easier. Potential applications are promising in condensation enhancement, window cleaning, photovoltaic panel cleaning, etc.

Although the whole study is based on a vertical surface driven by sinusoidal vibration, it can be extended to other situations. First, by simply replacing F_g by $F_g = m_d g \sin\alpha$, the developed model remains valid for inclined surfaces with an inclination angle α. Second, other forcing functions, such as triangle, square, or sawtooth, can also induce droplet coalescence as they can be treated as a series of sinusoidal functions by the Fourier expansion.

ACKNOWLEDGMENTS

The authors would like to acknowledge technical support from Frédéric Filaine. Special thanks to Dr. Eric Herbert for providing the vibration actuator, to Dr. John Lomas, and Dr. Philippe Brunet for their suggestions on the manuscript. Xiangshu Lei received financial support from the CSC (China Scholarship Council). This work was also supported by the National Natural Science Foundation of China (Grant No. 52006164).

AUTHOR DECLARATIONS

Conflict of Interest

The authors have no conflicts to disclose.

Author Contributions

Xiangshu Lei: Data curation (equal); Formal analysis (equal); Visualization (equal); Writing – original draft (equal). **Yingwen Liu:** Funding acquisition (equal); Supervision (equal). **Peng Yang:** Project administration (supporting); Supervision (supporting). **Laurent Royon:** Conceptualization (equal); Resources (equal). **Xiaofeng Guo:** Conceptualization (equal); Formal analysis (equal); Funding acquisition (equal); Investigation (equal); Methodology (equal); Supervision (equal); Validation (equal); Writing – review & editing (equal).

DATA AVAILABILITY

The data that support the findings of this study are available from the corresponding authors upon reasonable request.

REFERENCES

[1]X. Li, Y. Li, R. Cai, C. Yan, X. Qiao *et al.*, "Insufficient condensable organic vapors lead to slow growth of new particles in an urban environment," Environ. Sci. Technol. **56**, 9936–9946 (2022).
[2]B. E. Fil, G. Kini, and S. Garimella, "A review of dropwise condensation: Theory, modeling, experiments, and applications," Int. J. Heat Mass Transfer **160**, 120172 (2020).
[3]T. G. G. Uthpala, S. B. Navaratne, and A. Thibbotuwawa, "Review on low-temperature heat pump drying applications in food industry: Cooling with dehumidification drying method," J. Food Process Eng. **43**, e13502 (2020).
[4]A. Parker and C. Lawrence, "Water capture by a desert beetle," Nature **414**, 33–34 (2001).
[5]B. Yang, G. Shen, H. Chen, Y. Feng, and L. Wang, "Experimental study of condensation heat-transfer and water-recovery process in a micro-porous ceramic membrane tube bundle," Appl. Therm. Eng. **155**, 354–364 (2019).
[6]F. Macedonio, M. Frappa, A. Brunetti, G. Barbieri, and E. Drioli, "Recovery of water and contaminants from cooling tower plume," Environ. Eng. Res. **25**, 222–229 (2019).
[7]A. Sadeghpour, Z. Zeng, H. Ji, N. D. Ebrahimi, A. L. Bertozzi, and Y. S. Ju, "Water vapor capturing using an array of traveling liquid beads for desalination and water treatment," Sci. Adv. **5**, eaav7662 (2019).
[8]J. W. Rose, "Dropwise condensation theory and experiment: A review," Proc. Inst. Mech. Eng., Part A **216**, 115–128 (2002).
[9]P.-B. Bintein, H. Lhuissier, A. Mongruel, L. Royon, and D. Beysens, "Grooves accelerate dew shedding," Phys. Rev. Lett. **122**, 098005 (2019).
[10]C. Dorrer and J. Rühe, "Wetting of silicon nanograss: From superhydrophilic to superhydrophobic surfaces," Adv. Mater. **20**, 159–163 (2008).
[11]J. B. Boreyko and C.-H. Chen, "Self-propelled dropwise condensate on superhydrophobic surfaces," Phys. Rev. Lett. **103**, 184501 (2009).
[12]X. Liu, J. Trosseille, A. Mongruel, F. Marty, P. Basset, J. Laurent, L. Royon, T. Cui, D. Beysens, and T. Bourouina, "Tailoring silicon for dew water harvesting panels," iScience **24**, 102814 (2021).
[13]R. Wen, S. Xu, X. Ma, Y.-C. Lee, and R. Yang, "Three-dimensional superhydrophobic nanowire networks for enhancing condensation heat transfer," Joule **2**, 269–279 (2018).
[14]J. Y. Ho, K. F. Rabbi, S. Khodakarami, J. Ma, K. S. Boyina, and N. Miljkovic, "Opportunities in nano-engineered surface designs for enhanced condensation heat and mass transfer," J. Heat Transfer **144**, 050801 (2022).
[15]R. Enright, N. Miljkovic, A. Al-Obeidi, C. V. Thompson, and E. N. Wang, "Condensation on superhydrophobic surfaces: The role of local energy barriers and structure length scale," Langmuir **28**, 14424–14432 (2012).
[16]M. Costalonga and P. Brunet, "Directional motion of vibrated sessile drops: A quantitative study," Phys. Rev. Fluids **5**, 023601 (2020).
[17]H. B. Eral, D. J. C. M. 't Mannetje, and J. M. Oh, "Contact angle hysteresis: A review of fundamentals and applications," Colloid Polym. Sci. **291**, 247–260 (2013).
[18]H. Butt, J. Liu, K. Koynov, B. Straub, C. Hinduja, I. Roismann, R. Berger, X. Li, D. Vollmer, W. Steffen, and M. Kappl, "Contact angle hysteresis," Curr. Opin. Colloid Interface Sci. **59**, 101574 (2022).
[19]M. Moradi, S. F. Chini, and M. H. Rahimian, "Vibration-enhanced condensation heat transfer on superhydrophobic surfaces: An experimental study," AIP Adv. **10**, 095123 (2020).
[20]K. Sun, L. Shu, F. Jia, Z. Li, and T. Wang, "Vibration-induced detachment of droplets on superhydrophobic surfaces," Phys. Fluids **34**, 053319 (2022).
[21]I. Oh, H. Cha, J. Chen, S. Chavan, H. Kong, N. Miljkovic, and Y. Hu, "Enhanced condensation on liquid-infused nanoporous surfaces by vibration-assisted droplet sweeping," ACS Nano **14**, 13367–13379 (2020).
[22]C. P. Migliaccio, "Resonance-induced condensate shedding for high-efficiency heat transfer," Int. J. Heat Mass Transfer **79**, 720–726 (2014).
[23]R. A. Huber and M. M. Derby, "Droplet coalescence and departure on a vibrating film during humid air condensation," in *15th International Conference on Nanochannels, Microchannels, and Minichannels, New York, August 27–30, 2017* (ASME, 2017).
[24]L. Zhang, J. Shi, B. Xu, and Z. Chen, "Experimental study on distribution characteristics of condensate droplets under ultrasonic vibration," Microgravity Sci. Technol. **30**, 737–746 (2018).

[25]C. A. Schneider, W. S. Rasband, and K. W. Eliceiri, "NIH image to ImageJ: 25 years of image analysis," Nat. Methods **9**, 671–675 (2012).
[26]The MathWorks Inc., *MATLAB Version: 9.9.0 (R2020b)* (The MathWorks Inc., Natick, MA, 2020).
[27]K. Sarkar and W. R. Schowalter, "Deformation of a two-dimensional viscoelastic drop at non-zero Reynolds number in time-periodic extensional flows," J. Non-Newtonian Fluid Mech. **95**, 315 (2000).
[28]K. Sarkar and W. R. Schowalter, "Deformation of a two-dimensional drop at non-zero Reynolds number in time-periodic extensional flows: Numerical simulation," J. Fluid Mech. **436**, 177 (2001).
[29]Y. Yonemotoa and T. Kunugib, "Estimating critical surface tension from droplet spreading area," Phys. Lett. A **384**, 126218 (2020).
[30]F. Celestini and R. Kofman, "Vibration of submillimeter-size supported droplets," Phys. Rev. E **73**, 041602 (2006).
[31]M. Sellier, V. Nock, C. Gaubert, and C. Verdier, "Droplet actuation induced by coalescence: Experimental evidences and phenomenological modeling," Eur. Phys. J. **219**, 131–141 (2013).
[32]P. B. Weisensee, Y. Wang, H. Qian, D. Schultz, W. P. King, and N. Miljkovic, "Condensate droplet size distribution on lubricant-infused surfaces," Int. J. Heat Mass Transfer **109**, 187–199 (2017).
[33]H. K. Seong, "Fabrication of superhydrophobic surfaces," J. Adhes. Sci. Technol. **22**, 235–250 (2008).
[34]P. M. Somwanshi, P. K. Muralidhar, and S. Khandekar, "Coalescence of vertically aligned drops over a superhydrophobic surface," Phys. Fluids **32**, 052106 (2020).